The leading-edge vortex of yacht sails

THE LEADING-EDGE VORTEX OF YACHT SAILS

I. M. Viola, Institute for Energy Systems, School of Engineering, University of Edinburgh, UK, i.m.viola@ed.ac.uk
A. Arredondo-Galeana, Institute for Energy Systems, School of Engineering, University of Edinburgh, UK, a.arredondo@ed.ac.uk

It has been suggested that a stable Leading Edge Vortex (LEV) can be formed from the sharp leading edge of asymmetric spinnakers. If the LEV remains stably attached to the leading edge, it provides an increase in the thrust force. Until now, however, the existence of a stable and attached LEV has only been shown by numerical simulations. In the present work we experimentally verify, for the first time, that a stable LEV can be formed on an asymmetric spinnaker. We tested a 3D printed rigid sail in a water flume at a chord-based Reynolds number of ca. 10^4. The sail was tested in isolation (no hull and rigging) at an incidence with the flow equivalent to an apparent wind angle of $55°$ and a heel angle of $10°$. The flow field was measured with particle image velocimetry over horizontal cross sections. We found that on the leeward side of the sail, the flow separates at the leading edge reattaching further downstream and forming a stable LEV. The LEV grows in diameter from the root to the tip of the sail, where it merges with the tip vortex. We detected the LEV using the γ_1 and γ_2 criteria, and we verified its stability over time. The lift contribution provided by the LEV was computed solving a complex potential model of each sail section. This analysis showed that the LEV provides more than 10% of the total sail's lift. These findings suggests that the performance of asymmetric spinnakers could be significantly enhanced by promoting a stable LEV.

1 INTRODUCTION

Sails are thin wings with a relatively sharp leading edge. On headsails, where the leading edge is not attached to the mast, the sharp leading edge leads to flow separation at any non-zero angle of attack. This is one of the key features of yacht sails that makes them different from conventional wings. While wing designers try to prevent flow separation, in sail aerodynamics flow separation is a fact. Flow reattachment occurs somewhere downstream of the leading edge, forming a region of separated flow. This region is short in the chordwise direction, but it extends from the base to the tip. On downwind sails, the flow separates again before reaching the trailing edge; this is known as trailing edge separation. This larger separated region that could cover more than half of the chord, is easier to identify than the smaller leading edge separated region. Therefore, the extent of this rear region is typically used to inform the sail designer on where the sails' shape can be enhanced. However, virtually all of the driving force is generated near the leading edge. Thus small changes in the fluid dynamics of the leading edge separated region can result in significant gains in performance. This work aims to gain new insight on the flow in this region.

The flow separates at the leading edge, forming a strong separated shear layer. This results in the production of vorticity. At the typical Reynolds numbers (Re) of a yacht sail, from 5×10^5 to 5×10^7, the vorticity dissipation due to the viscosity is negligible. Therefore, the vorticity is accumulated in the separated region. The integral of the vorticity in this region leads to a circulation that has the same sign as the circulation of the sail; thus this vorticity contributes to the generation of lift. However, vorticity cannot be accumulated indefinitely. It can be either shed downstream with the main flow stream, or it must be somehow extracted. These two mechanisms are employed by the laminar separation bubble (LSB) and the leading edge vortex (LEV), respectively.

1.1 THE LAMINAR SEPARATION BUBBLE

The LSB occurs on the suction side of thin airfoils at transitional Reynolds numbers ($10^4 < Re < 10^6$). The laminar boundary layer that has grown from the leading edge, separates due to the adverse pressure gradient somewhere downstream of the foil's suction peak. The resulting separated shear layer promotes the laminar to turbulent transition and the generation of vorticity. The vorticity is continuously shed downstream in the form of vortices that roll on the surface of the airfoil toward the trailing edge. The time-averaged flow field shows flow reattachment downstream of the point where laminar to turbulent transition occurs. A thick turbulent boundary layer grows downstream of the reattachment point. This results in lower suction and lift, and also in higher momentum deficit in the wake and drag. A LSB-type of flow with continuous shedding of vorticity occurs at the leading edge of genoas and jibs [1, 2].

1.2 THE LEADING EDGE VORTEX

The LEV is a coherent vortex formed by the roll up of vorticity, generated at the leading edge. The vorticity is not continuously shed downstream, but is instead convected towards the centre of the vortex. If the vorticity is somehow extracted from the axis of the vortex, it is possible to achieve a stable LEV that remains attached to the leading edge indefinitely. The vorticity is typically extracted by axial flow inside of the vortex core, in the direction of the wing tip. A stable LEV grows in the direction in which the vorticity is extracted. The vorticity and circulation of the LEV can significantly increase the lift and thus it is exploited on both man-made and natural flyers [3, 4, 5, 6]. Remarkably, it has been identified across a wide range of Re. In laminar flow conditions, it has been found on autorotating seeds [7] and on the wings of insects [8] and small birds [9]. In transitional and turbulent flow conditions, it has been found on larger bird wings [10], fish fins [11] and delta wings [12, 13]. In helicopter rotors [14] and wind turbines [15], the LEV is a powerful but undesirable flow feature. This is due to the large angle of attack oscillations. At every period, the LEV is shed downstream leading to a lift overshoot above the quasi-static maximum lift and to an abrupt, and dangerous change in the pitch moment. Conversely, in biological flyers and delta wings, the LEV provides an essential source of lift augmentation.

Recent Detached Eddy Simulations (DES) [16] have revealed that a stable attached LEV might also occur on the asymmetric spinnakers of sailing yachts. This was anecdotally anticipated by Bethwaite [17], who sketched the LEV on the gennaker of a skiff. This exiting finding is the motivation for this work. In fact, the exploitation of the LEV by design has enabled a step change in the performance of a wide range of applications, from micro aerial vehicles to rockets and supersonic planes [13]. The understanding of how to promote and stabilise the LEV on downwind sails can enable a major step in the sails' performances. In this study, therefore, we aim to prove experimentally the existence of the LEV on a downwind sail, to identify its main features, and to quantify its contribution to sails' performances.

1.3 A BENCHMARK FOR DOWNWIND SAILS

The asymmetric spinnaker where the LEV was identified with DES [16] is considered in this work. The aerodynamics of this sail have been widely investigated in the last decade and this makes it one of the best available benchmarks for downwind sails. The geometry and the experimental, and numerical data are available on www.ignazioviola.com. This sail was designed for the AC33 class, which was proposed for the 33$^{\text{rd}}$ America's Cup. This class has never been adopted, as the 33$^{\text{rd}}$ America's Cup was eventually disputed under the Deed of Gift. A 1:15$^{\text{th}}$-scale model of this sail was tested in a wind tunnel at 55° AWA and 10° heel angle. The forces [18] and pressures [19] on the sail surfaces were recorded for a range of sail trims, and also compared with those measured on similar sails. The sail trim that allowed the maximum driving force, was used to build a rigid sail with embedded pressure taps and both forces, and pressures were measured in a wind tunnel [20]. This sail trim was also modelled with Reynolds-averaged Navier-Stokes (RANS) simulations [21] and with DES [16]. A 1:3$^{\text{rd}}$-scale prototype was built and tested on water on a Platu25-class yacht [22], where surface pressures were measured. A tri-way comparison between the pressures measured in a wind tunnel, on water and with RANS was presented in Viola and Flay [21]. While a comparison between wind tunnel tests performed with flexible and rigid sails, and DES, was presented in both [20] and [16]. The pressures from these three approaches showed a qualitative agreement, with the pressures computed numerically lying in between those measured with the two experimental techniques.

1.4 OVERVIEW OF THE PRESENT WORK

In order to test in highly controlled flow conditions and to identify the main mechanisms enabling the formation, and stability of the LEV, we tested the asymmetric spinnaker in isolation (without the mainsail and the hull), in low Re conditions. The Reynolds number based on the sail chord measured on a section at 3/4$^{\text{th}}$ of the mitre (measured from the sail's base) is $Re = 1.3 \times 10^4$. The actual flow of a real sail is certainly more complex than the one of this simplified model. The effects of the mainsails are primarily to generate upwash and to increase the effective angle of attack. Therefore, their effects can be mostly accounted for by adjusting the angle of attack. We do not take into account the effects of the enhanced turbulent mixing and boundary layer effects at higher Reynolds numbers. However, the LEV has been found to be very resilient to the effects of Reynolds numbers [23]. Therefore, while this investigation does not provide a quantitative description of the full-scale flow, it enables the understanding of the key features of downwind sail flow.

The rest of the paper is organised as follows: in Section 2, Methodology, we present the details of the methodology, including the geometry of the sail, the experimental rig, the flow conditions, the instrumentation used to measure the flow field and how we analysed the data. In Section 3, Results, we present the flow measurements, the analysis of the LEV and an estimate of the contribution of the LEV to the sail's performance. Finally, in Section 4, Conclusions, we summarise the key findings.

2 METHODOLOGY

2.1 SAIL MODEL

The geometry of the 3D-printed model used for this investigation is available on www.ignazioviola.com. The model has an area of $A = 0.045\,\text{m}^2$. The twist angle from the base to the head is 16°, the maximum chordwise camber is $0.40c_0$ and the maximum spanwise camber is $0.65c_0$, where $c_0 = 0.114\,\text{m}$ is the chord of a sail section at 3/4$^{\text{th}}$ of the span from the base Fig. (1).

The model is 3 mm thick. Separation at the leading edge is promoted chamfering the edges. The chamfer at the leading and trailing edges is 20° for the first 3/4$^{\text{th}}$ of the span from the base to the head. At the top 1/4$^{\text{th}}$ of the sail's span, the chamfer grows progressively from 20° to 70°, allowing the

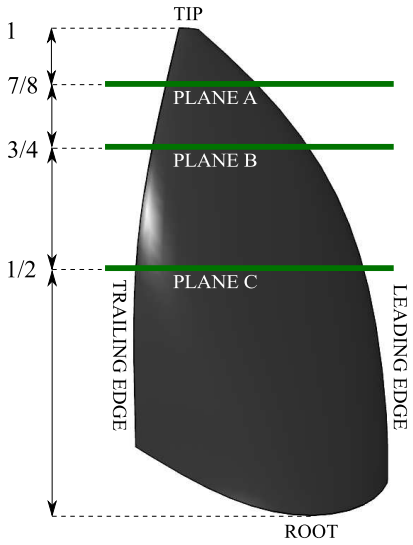

Figure 1: Rendering of the sail model and position of the measurement planes.

thickness to remain constant on the mitre. The head of the sail is blunt.

The model was 3D printed in ABS with a Fortus 250 3D printer. The model was mounted on a rotating shaft controlled by a lever arm for the fine control of the angle of attack. The shaft was attached to a 6 mm thick acrylic plate connected to a pair of $45 \times 45\,\mathrm{mm}$ aluminium extrusions attached to the flume's side walls. The rig allows to change the angle of attack and to secure its testing position through an arch dial system (Fig. 2). The shaft was set to replicate the same AWA ($55°$) and heel angle ($10°$) as tested with DES by [16].

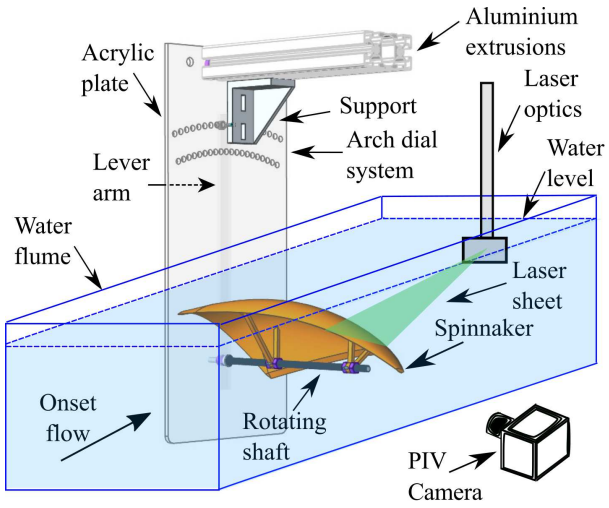

Figure 2: Schematic diagram of the experimental setup.

2.2 WATER FLUME

The water flume is a current-wave testing facility in the Institute of Engineering Systems of the School of Engineering, University of Edinburgh. It is $2\,\mathrm{m}$ long, $0.4\,\mathrm{m}$ wide and $0.9\,\mathrm{m}$ high. The water depth was set to $0.5\,\mathrm{m}$ and the sail was placed horizontally $0.1\,\mathrm{m}$ below the water surface. The free space between the rig and the walls of the flume was $0.05\,\mathrm{m}$ at both sides. The model was tested in a uniform current with $U_\infty = 0.1146\,\mathrm{m/s}$. A turbulence intensity of 7% was measured with Laser Doppler Velocimetry $1\,\mathrm{m}$ upstream of the model.

2.3 PARTICLE IMAGE VELOCIMETRY

We used a Particle Image Velocimetry (PIV) system consisting of a Solo 200XT pulsed dual-head Nd:YAG laser, with an energy output of 200 mJ at a wavelength of $\lambda = 532\,\mathrm{nm}$. In addition, one CCD Imperx 5MP camera with a $2448\,\mathrm{px} \times 2050\,\mathrm{px}$ resolution and a Nikkor f/2, 50 mm lense were used. The seeding particles were silver coated hollow glass spheres with an average diameter of $14\,\mu\mathrm{m}$ and a density of $1.7\,\mathrm{g/cc}$. In order to mitigate surface reflections, a coating of matt black paint was applied to the sail with a second coating of rhodamine B. A third coating of acrylic was applied to protect the rhodamine B coating from water. An optical filter was used on the camera to subtract the wavelength of rhodamine B and minimise the reflected light. Additionally, background subtraction was performed [24] that allowed measurements to be made in close proximity to the wall. The leading edge region, however, was not affected by laser reflections due to the curvature of the sail and the direction of the laser sheet.

The laser beam was redirected through two mirrors and an array of underwater LaVision optics to generate a laser sheet parallel to the flow. The laser sheet was fully submerged as shown in Fig. 2. The thickness of the laser sheet was approximately $2\,\mathrm{mm}$. Three cross sections of the sail were recorded: plane A, B and C. These are located respectively at $^7/_8$, $^3/_4$ and $^1/_2$ of the distance from the root of the sail to the tip (Fig. 1).

PIV pair images were sampled at 7.5 Hz. A two pass adaptive correlation was applied. The first pass had a $64\,\mathrm{px} \times 64\,\mathrm{px}$ interrogation window, with a Gaussian weighting and 50% window overlap. The second pass had a $24\,\mathrm{px} \times 24\,\mathrm{px}$ interrogation window and a 75% window overlap. Averaged fields were generated from the full time series and a 3×3 filter was used to smoothen the vector fields.

2.4 VORTEX DETECTION CRITERIA

The γ_1 and the γ_2 vortex detection criteria were developed by [25] to overcome the intermittence due to low-scale turbulence of methods that rely, on local quantities such as velocity gradients or vorticity. The method is defined as a non-local scheme by [26] and has been applied successfully to PIV data (e.g. [27, 28] and [29]). The γ_2 criterion is the non-Galilean invariant version of the γ_1 criterion, as the local convection velocity is subtracted. Figure 3 shows a schematic drawing of the γ_1 algorithm. The γ_1 criterion at a point P is computed using the PIV data within a square window S of size $2l \times 2l$ centred in P. At each point M within S, the sine of the angle θ_M between the vector $\mathbf{PM}$ and the velocity $\mathbf{u}_\mathrm{M}$ is computed.

The γ_1 value in P is given by

$$\gamma_1 = \frac{1}{N}\sum_S \frac{\mathbf{PM}\times\mathbf{u}_\mathrm{M}}{||\mathbf{PM}||\cdot||\mathbf{u}_\mathrm{M}||} = \frac{1}{N}\sum_S \sin(\theta_\mathrm{M}), \qquad (1)$$

where N is the number of grid points in S.

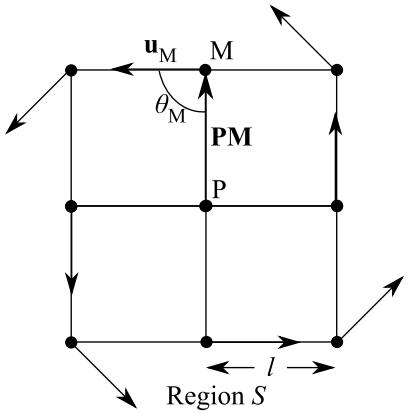

Figure 3: Vortex detection algorithm.

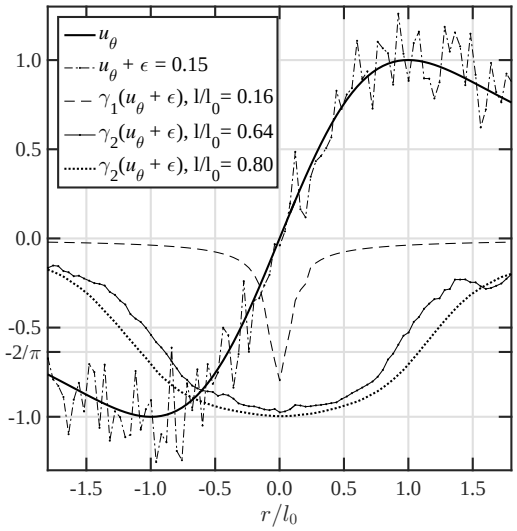

Figure 4: γ_1 and γ_2 criteria for a Lamb-Oseen vortex.

In the γ_2 criterion, the average convection velocity $\langle\mathbf{u}\rangle$ in the region S is subtracted from every velocity point in the interrogation window, such that

$$\gamma_2 = \frac{1}{N}\sum_S \frac{\mathbf{PM}\times(\mathbf{u}_\mathrm{M}-\langle\mathbf{u}\rangle)}{||\mathbf{PM}||\cdot||\mathbf{u}_\mathrm{M}-\langle\mathbf{u}\rangle||}, \qquad (2)$$

where

$$\langle\mathbf{u}\rangle = \frac{1}{N}\sum_S \mathbf{u}_\mathrm{M}. \qquad (3)$$

2.5 CALIBRATION OF THE VORTEX DETECTION CRITERIA

To calibrate the vortex detection criteria, the γ_1 and γ_2 algorithms are implemented for an isolated Lamb-Oseen vortex. The tangential velocity of the Lamb-Oseen vortex is

$$u_\theta = \frac{\Gamma}{2\pi r}\left(1-\exp\left(-\frac{r^2}{l_0^2}\right)\right), \qquad (4)$$

where Γ is the strength of the vortex, r is the radial coordinate and l_0 is the core vortex size, defined as the radial coordinate where the tangential velocity is maximum.

The γ_1 and γ_2 criteria for the Lamb-Oseen vortex are shown in Fig. 4. The γ_2 criterion is computed for two different sizes l of the interrogation window S: $l/l_0 = 0.64$ and 0.80; for γ_1, $l/l_0 = 0.16$. The centre of the vortex is identified by the maximum of both the γ_1 and γ_2 criteria, while the radius of the vortex core is identified by $|\gamma_2| = 2/\pi$.

A random error $\epsilon = 15\%\, u_\theta$ is included to model the effect of PIV noise that is generated during acquisition and post-processing [26]. A 15% noise in γ_1 is found to decrease the magnitude of the detection peak by 30%. When l/l_0 decreases, γ_2 shows greater fluctuations and it behaves more like a local criterion. This leads to the underestimation of the vortex core size. For the γ_1 criterion, the smaller the l/l_0 is set, the narrower the detection peak becomes [25].

In the present experiment, the LEV core size is found to be ca. $l_0 = 0.1c$. The size l of the interrogation window is set to $l/l_0 = 0.16$ and 0.80 for γ_1 and γ_2, respectively. The noise level in the experiment is estimated to be ca. $15\%\, u_\theta$. In fact, the maximum $|\gamma_1|$ on the sail was 0.7.

2.6 COMPLEX POTENTIAL MODEL

In order to estimate the contribution of the LEV to the lift of the sail, a potential flow model of a circular arc is developed. This has the same chord c and maximum camber 2μ than the considered sail's section, and it experiences a uniform flow with the same free stream velocity U_∞ and angle of attack α with respect to the chord. The arc can be mapped onto a rotating circular cylinder that has the same circulation and lift than the arc. The cylinder is defined in the complex plane ζ, where the complex coordinate

$$\zeta \equiv X + iY \equiv re^{i\theta} \qquad (5)$$

identifies a position vector in the Cartesian coordinates (X, Y) and in the polar coordinates (r, θ). The velocity potential $\phi = \phi(\zeta)$ and the stream function $\psi = \psi(\zeta)$ are such that the velocity in the $X-$direction is

$$U \equiv \frac{\partial\phi}{\partial X} \equiv \frac{\partial\psi}{\partial Y}, \qquad (6)$$

and the velocity in the $Y-$direction is

$$V \equiv \frac{\partial\phi}{\partial Y} \equiv -\frac{\partial\psi}{\partial X}. \qquad (7)$$

The complex potential is

$$F(\zeta) \equiv \phi(\zeta) + i\psi(\zeta), \qquad (8)$$

and the complex velocity is

$$W(\zeta) \equiv \frac{\partial F(\zeta)}{\partial \zeta} = U - iV. \tag{9}$$

The complex velocity provides the velocity field around the rotating cylinder. The cylinder is centred in $\zeta_0 = \mu e^{i\pi/2} = i\mu$ and has a radius $R = c/(4\cos\beta)$, where $\beta = \arctan(4\mu/c)$ and the maximum camber is 2μ (Fig. 5).

The velocity field in the ζ plane of the cylinder can be mapped onto the plane $\hat{z}$ of the circular arc with the Joukowski transformation

$$\hat{z} = \zeta + \frac{(R\cos\beta)^2}{\zeta}. \tag{10}$$

In the $\hat{z}$ plane, the coordinate system is centred in the middle of the chord, such that the $\hat{x}-$axis is in the direction of the chord and positive toward the trailing edge, and the $\hat{y}-$axis is positive toward the suction side.

Finally, a further transformation

$$z = \hat{z}e^{-i\alpha} \tag{11}$$

allows a description of the flow field in the flume reference system, where the $x-$axis is aligned with the free stream velocity U_∞. These two transformations are shown in Fig. 6.

The complex potential of the cylinder in the ζ plane is

$$F_0(\zeta) = U_\infty(\zeta - \zeta_0)e^{-i\alpha} + \frac{U_\infty R^2 e^{i\alpha}}{\zeta - \zeta_0} - \frac{i\Gamma_0}{2\pi}\ln(\zeta - \zeta_0), \tag{12}$$

where

$$\Gamma_0 = -4\pi U_\infty R\sin(\alpha + \beta) \tag{13}$$

is the circulation of the cylinder. Circulation values are defined positive anticlockwise.

The LEV can be modelled as a free vortex in the ζ plane. The circulation of the free vortex Γ_{LEV} is computed from the measured flow field, as the integral of the tangential velocity over the closed iso-line l of the γ_2 criterion, where $\gamma_2 = 0.70$:

$$\Gamma_{\mathrm{LEV}} = \oint_{|\gamma_2|=0.70} \mathbf{u}\cdot \mathrm{dl}. \tag{14}$$

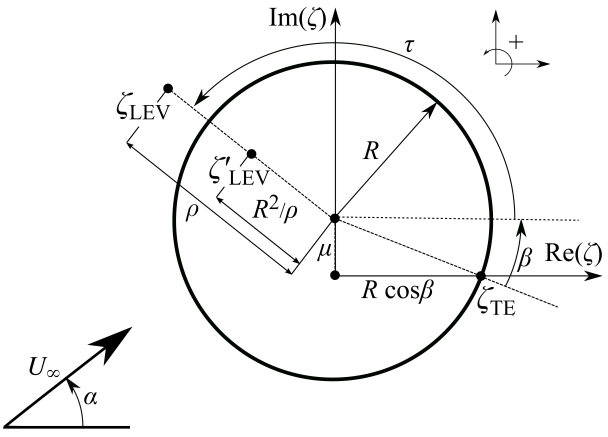

Figure 5: Complex potential model in the ζ plane.

The coordinates of the centre of the LEV, determined with the γ_2 criteria, are used to compute its polar coordinates in terms of ρ and τ in the ζ plane

$$\zeta_{LEV} = \rho e^{i\tau} + \mu e^{i\pi/2}. \tag{15}$$

If only one free vortex was added, the cylinder would no longer be impermeable and in the $\hat{z}$ plane, the Kutta condition would not be satisfied at the trailing edge. In order to restore the impermeability of the cylinder, a mirror vortex with circulation $-\Gamma_{\mathrm{LEV}}$ must be placed inside of the cylinder at the inverse square point

$$\zeta'_{LEV} = \frac{R^2}{\rho}e^{i\tau} + \mu e^{i\pi/2}. \tag{16}$$

To cancel the circulation of the mirror vortex $-\Gamma_{\mathrm{LEV}}$, the bound circulation of the cylinder is increased by Γ_{LEV}. Moreover, to satisfy the Kutta condition, the bound circulation of the cylinder Γ_b must be different from the circulation Γ_0 of the cylinder in isolation. The total circulation inside of the boundary of the cylinder is $\Gamma_b - \Gamma_{\mathrm{LEV}} + \Gamma_{\mathrm{LEV}} = \Gamma_b$.

The resulting complex potential is

$$\begin{aligned} F(\zeta) = {} & U_\infty(\zeta - \zeta_0)e^{-i\alpha} \\ & + \frac{U_\infty R^2 e^{i\alpha}}{(\zeta - \zeta_0)} - \frac{i(\Gamma_\mathrm{b} + \Gamma_{\mathrm{LEV}})}{2\pi}\ln(\zeta - \zeta_0) \\ & - \frac{i\Gamma_{\mathrm{LEV}}}{2\pi}\ln\frac{\zeta - \zeta_{\mathrm{LEV}}}{\zeta - \zeta'_{\mathrm{LEV}}}. \end{aligned} \tag{17}$$

where the first line is the contribution of the free stream, the second line is due to the cylinder and the circulation in the centre of the cylinder and the third line is due to the free vortices in ζ_{LEV} and ζ'_{LEV}. By derivation of the complex potential, we compute the complex velocity as

$$\begin{aligned} W(\zeta) = {} & U_\infty e^{-i\alpha} \\ & - \frac{U_\infty R^2 e^{i\alpha}}{(\zeta - \zeta_0)^2} - \frac{i(\Gamma_\mathrm{b} + \Gamma_{\mathrm{LEV}})}{2\pi}\frac{1}{\zeta - \zeta_0} \\ & - \frac{i\Gamma_{\mathrm{LEV}}}{2\pi}\frac{\zeta - \zeta'_{\mathrm{LEV}}}{\zeta - \zeta_{\mathrm{LEV}}}. \end{aligned} \tag{18}$$

Having derived the complex velocity for a generic Γ_b, it is now possible to compute the Γ_b that satisfies the Kutta condition. The ζ_{TE} coordinate, corresponding to the trailing edge of the circular arc in the $\hat{z}$ plane, must be a stagnation point of the cylinder. Using Eq. (18) to evaluate $W(\zeta = \zeta_{TE}) = 0$, we find that

$$\Gamma_b = \Gamma_0 - \kappa\Gamma_{\mathrm{LEV}}, \tag{19}$$

where

$$\kappa \equiv \frac{1 - \frac{\rho}{R}\cos(\beta + \tau)}{\frac{1}{2}[(\frac{\rho}{R})^2 + 1] - \frac{\rho}{R}\cos(\beta + \tau)}. \tag{20}$$

is a geometric coefficient that takes into account the relative position of the LEV. Due to the proximity of the LEV to the surface of the circular arc, $\rho \approx R$ and thus $\kappa \approx 1$. This result shows that if the LEV introduces new circulation, the bound circulation must decrease by almost the same amount, i.e.

$$\Gamma_b + \Gamma_{\mathrm{LEV}} \approx \Gamma_0. \tag{21}$$

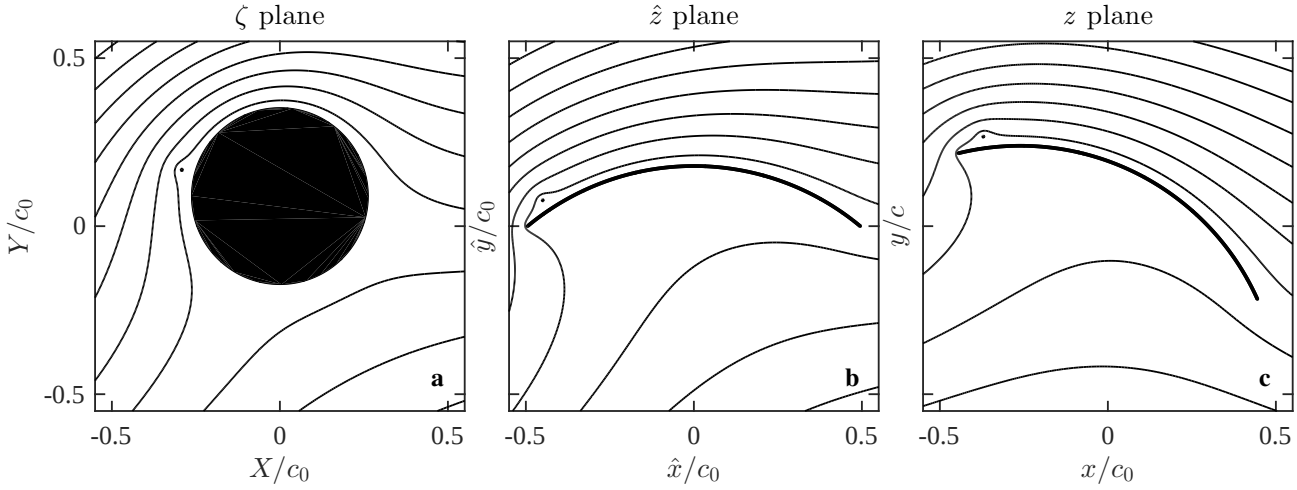

Figure 6: Velocity potential streamlines in the ζ plane (**a**) and the transformations in Eq. 10 (**b**) and Eq. 11 (**c**).

Using the Kutta-Joukowski theorem, the lift coefficient for the circular arc in the presence of the LEV is written as

$$C_L = -\frac{\Gamma_b + \Gamma_{\text{LEV}}}{\frac{1}{2}U_\infty c} = -\frac{\Gamma_b}{\frac{1}{2}U_\infty c} - \frac{\Gamma_{\text{LEV}}}{\frac{1}{2}U_\infty c}. \quad (22)$$

In the Results, the lift coefficient contribution due to the bound circulation

$$C_{L_b} \equiv -\frac{\Gamma_b}{\frac{1}{2}U_\infty c} \quad (23)$$

and the lift coefficient contribution due to the LEV

$$C_{L_{\text{LEV}}} \equiv -\frac{\Gamma_{\text{LEV}}}{\frac{1}{2}U_\infty c} \quad (24)$$

will be compared.

3 RESULTS

3.1 FLOW AND VORTICITY FIELDS

Figure 7 shows the time-averaged vector fields, streamlines and vorticity contours for the planes A, B and C. The local angle of attack increases from plane A to plane C due to the twist of the sail. The maximum camber also increases from plane A to plane C. Planes A and B show flow separation at the leading edge and flow reattachment further downstream. The leading edge vortex is shown by the concentric streamlines at the leading edge (Fig. 7e). The instantaneous wall normal velocity profiles (yellow lines in Figs. 7a and 7b) show reattachment downstream of the LEV in 90% of the image pairs. Differently to a laminar separation bubble (LSB), the separation of the LEV occurs at the leading edge and its diameter grows towards the tip of the sail (from plane C to plane A). The streamlines are concentric and swirl towards the centre of the vortex, where high speed flow is ejected along its axis of rotation.

On plane C, the flow remains attached at the leading edge but separates at $x/c = -0.3$ without reattaching. Vorticity contours show the shear layer generated at the leading edge for the three planes. The separated shear layer curves down in planes A (Fig. 7g) and B (Fig. 7h) showing the effect of the high circulation on these planes, while it is straighter on plane C (Fig. 7i) where trailing edge separation occurs.

3.2 VORTEX TOPOLOGY

The γ_2 contours for the instantaneous velocity fields of planes A, B and C are presented in Fig. 8. A sequence of 9 consecutive images is presented for a total period of time $\Delta t^* = 1.072$, where the time t is made non-dimensional with the chordwise convection period c_0/U_∞, i.e. $t^* \equiv tU_\infty/c_0$. The sequences are taken at different times on each plane, since the experimental setup does not allow simultaneous recording of the planes. On planes A and C, vortices are shed with a convective velocity of $0.6U_\infty$ in plane A and $0.3U_\infty$ in plane C. On planes A and B, a stable LEV that remains attached to the leading edge is observed. Indeed, the LEV on these planes is intermittently stable. For example, on plane B, during the sampling period of $0.000 < t^* < 40.736$, a stable LEV was found for $0.000 < t^* < 8.576$, $15.276 < t^* < 22.646$ and $35.242 < t^* < 40.736$.

Fig. 9 shows the γ_1 and γ_2 criteria on planes A and B, averaged over the course of the entire sampling period $0.000 < t^* < 40.736$. The vortex size grows from plane B (Fig. 9b) to plane A (Fig. 9a), i.e. in the direction of the tip which is where the vorticity is extracted. The γ_1 criterion has one global maximum at the centre of the LEV. The maximum γ_1 is 0.7 in plane A and 0.8 in plane B. Conversely, the γ_2 criterion has two local maxima on each plane. On plane A, the maxima are both 0.79. On plane B, these are 0.79 near the leading edge and 0.76 at ca. $x/c = -0.2$.

In Fig. 10, the γ_2 criterion is computed for the time-averaged flow fields corresponding to the sequence in Fig. 8, for a period $\Delta t^* = 1.072$. The region near the leading edge is zoomed in to give a closer look at the LEV on planes

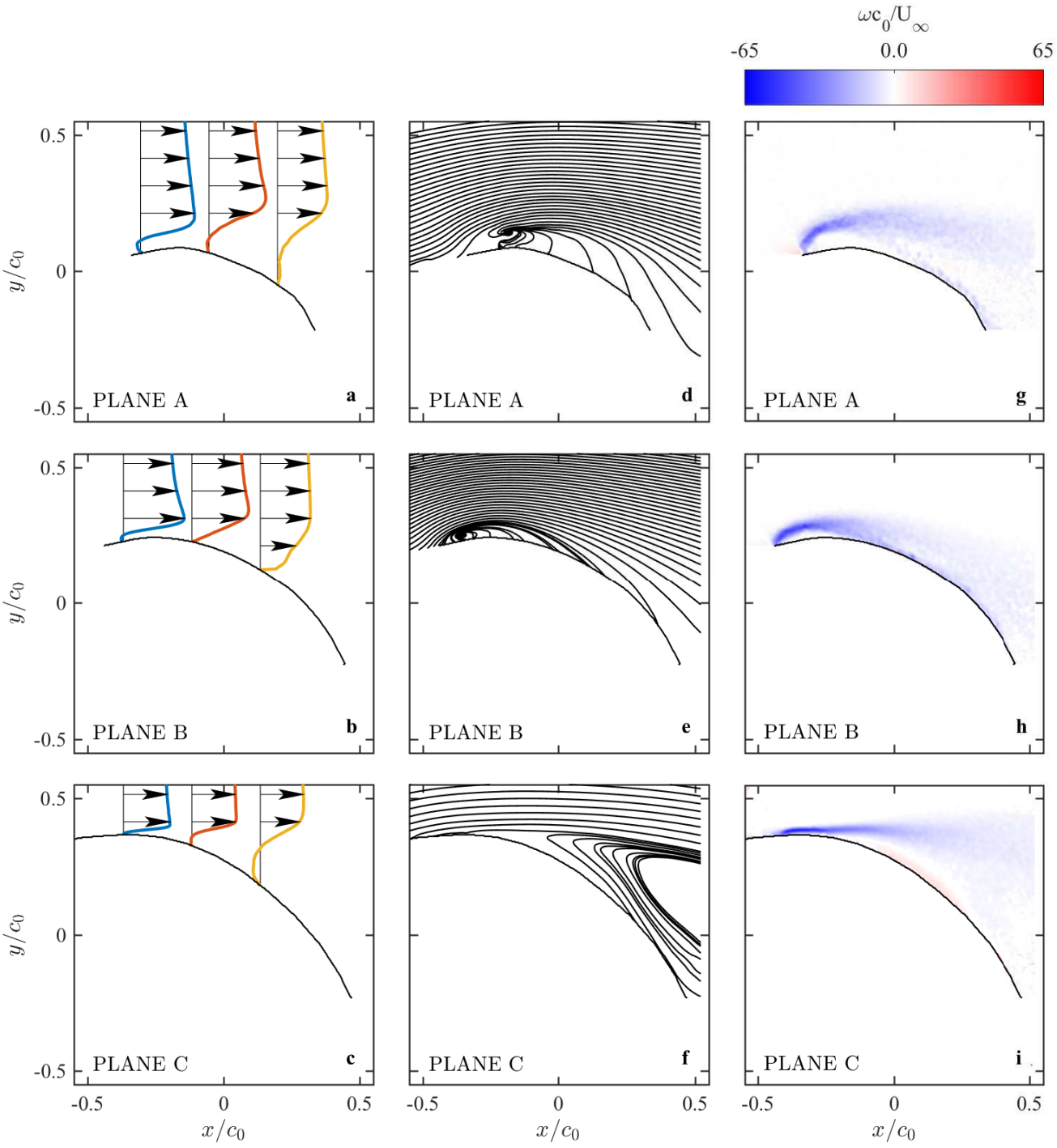

Figure 7: Time-averaged velocity profiles (**a, b, c**), streamlines (**d, e, f**) and contours of non-dimensional vorticity (**g, h, i**) on the planes A, B and C. Data is averaged over a period $0.000 < t^* < 40.736$.

A and B. On plane A, the γ_2 iso-lines with low value have an elongated shape, but the LEV has only one core near the leading edge. Conversely, on plane B, the LEV is split into two co-rotating cores, as on a dual LEV [30, 12].

3.3 COMPLEX POTENTIAL MODEL

The underlying question that this work aims to address, is the effective contribution of the LEV to the sail performance. Recalling that the total lift coefficient can be broken down into the contribution of the bound circulation C_{L_b} and the contribution of the LEV $C_{L_{\mathrm{LEV}}}$, the ratio $C_{L_{\mathrm{LEV}}}/C_{L_b} = \Gamma_{LEV}/\Gamma_b$ is computed. The conservative estimate is made that the Kutta

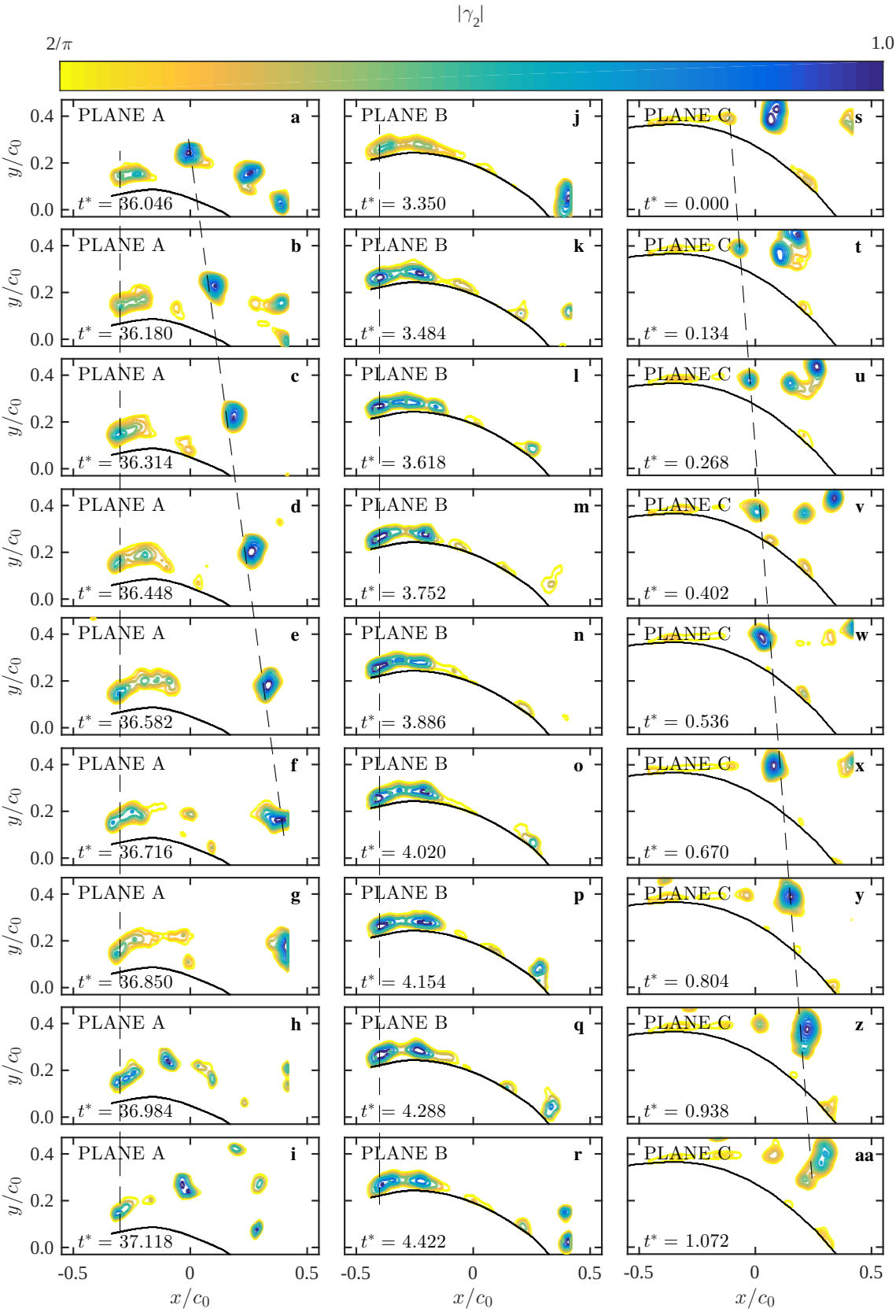

Figure 8: γ_2 criterion on instantaneous velocity fields for planes A (**a**-**i**), B (**j**-**r**) and C (**s**-**aa**). Data corresponds to a period of $\Delta t^* = 1.072$, in the interval $0.000 < t^* < 40.736$.

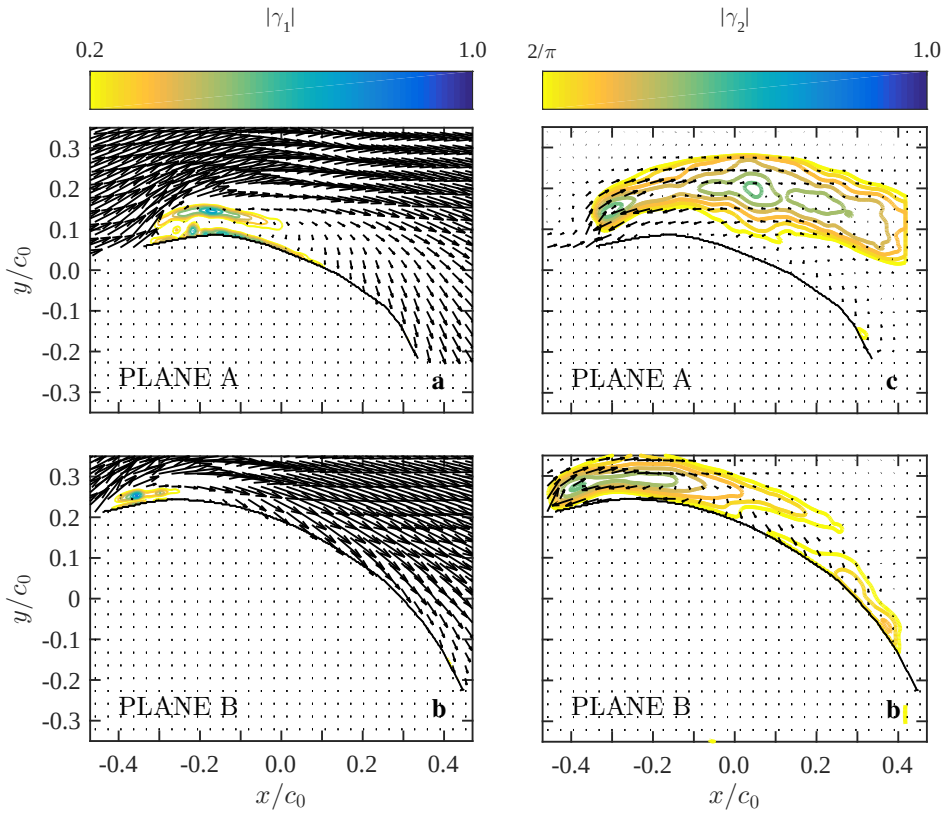

Figure 9: γ_1 and γ_2 criteria of the time-averaged velocity field measured for $0.000 < t^* < 40.736$ on the planes A and B.

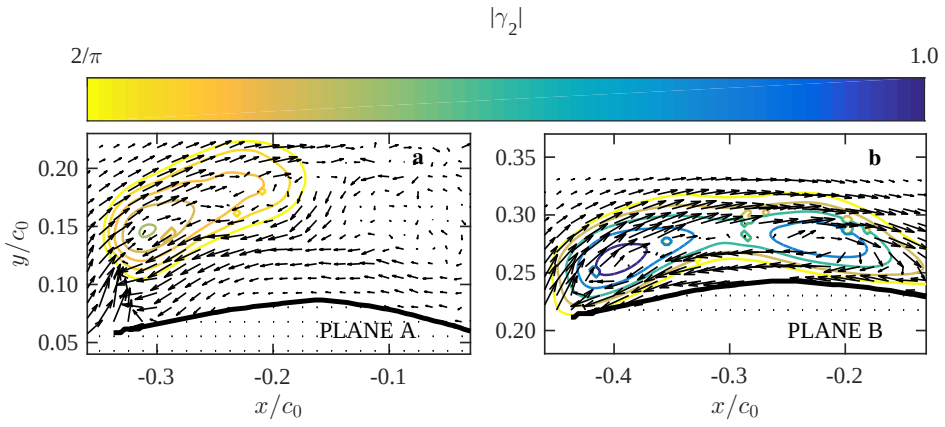

Figure 10: γ_2 criterion of the velocity field measured on planes A and B and time-averaged over the periods $\Delta t^* = 1.072$ presented in Fig. 8.

condition is satisfied when the LEV is present. Since trailing edge separation actually occurs and the Kutta condition is not satisfied, the computed bound circulation is higher than the real value.

The circulation of the LEV Γ_{LEV}, for plane A and plane B, is computed from Fig. 10 by integrating along the iso-line of $\gamma_2 = 0.7$, the flow velocity tangential to the iso-line. The bound circulation is computed from Eqs. 13, 19, and 20. Eqs. 19 and 20 show that Γ_b increases with the distance of the LEV from the sail (i.e. with ρ/c) and with the angle of attack α. Table 1 shows the experimental values of the different parameters that contributes to compute Γ_b. It can be seen that from plane A to plane B, ρ/c decreases but α increases, leading to two similar values of κ. It is found that $C_{L_{\mathrm{LEV}}}/C_{L_b} = \Gamma_{\mathrm{LEV}}/\Gamma_b = 0.07$ and 0.14 on planes A and B, respectively. Therefore, the contribution of the LEV is of paramount importance in the performances of the sails.

Table 1: Input values and results of the complex potential flow model for planes A and B.

	α	β	τ	$2\mu/c$	ρ/c	κ_{LEV}	Γ_{LEV}/Γ_b
Plane A	23^o	20^o	170^o	0.18	0.37	0.83	0.07
Plane B	26^o	20^o	165^o	0.18	0.27	0.93	0.14

4 CONCLUSIONS

Recent high-fidelity numerical simulations [16] suggested that a LEV is formed at the leading edge of asymmetric spinnakers and that it remains stably attached to the sail providing lift augmentation. This finding is investigated in the present paper. A model-scale asymmetric spinnaker is tested in uniform flow in a water flume. The Reynolds number based on the chord c_0 at 3/4$^{\text{th}}$ of the mitre and the free stream velocity U_∞ is 1.3×10^4. PIV shows that the LEV is absent or of negligible dimensions on the lower half of the sail, where trailing edge separation is dominant. The separation point is found well upstream of the mid-chord. On the higher half of the sail, the LEV is formed and it grows in size towards the head of the sail, where it merges with the tip vortex. Downstream of the LEV, the flow reattaches and a turbulent boundary layer is formed. The LEV remains attached to the leading edge intermittently. For a period of time of the order of $10c/U_\infty$, the LEV is stably attached, and then for a period of similar length the LEV is continuously shed. When the LEV is attached, its contribution to the lift on the upper half of the sail is between 7% and 14%. The contribution on the total lift could not be measured, but given that the majority of the lift is generated by the upper half of the sails, it is expected to be higher than 10%. More investigation on the LEV contribution to the lift force is ongoing. These results suggest that the performance of asymmetric spinnakers could be enhanced significantly by controlling the formation and stability of the LEV.

5 ACKNOWLEDGEMENTS

This work was funded by the Consejo Nacional de Ciencia y Tecnología (CONACYT).

REFERENCES

[1] I. M. Viola and R. G. J. Flay. Sail aerodynamics: Understanding pressure distributions on upwind sails. *Exp Therm and Fluid Sci*, 35(8):1497–1504, 2011. doi: 10.1016/j.expthermflusci.2011.06.009.

[2] I. M. Viola and R. G. J. Flay. Aerodynamics of headsails: a review of measured surface pressures and expected flow fields. In *5th High Performance Yacht Design Conference*, Auckland, New Zealand, 2015.

[3] C. P. Ellington. The novel aerodynamics of insect flight: applications to micro-air vehicles. *J Exp Biol*, 202(23): 3439–3448, 1999.

[4] R. B. Srygley and A. L. R. Thomas. Unconventional lift-generating mechanisms in free-flying butterflies. *Nature*, 420(6916):660–664, 2002. doi: 10.1038/nature01223.

[5] D. J. Garmann, M. R. Visbal, and P. D. Orkwis. Three-dimensional flow structure and aerodynamic loading on a revolving wing. *Phys Fluids*, 25(3), 2013. doi: 10.1063/1.4794753.

[6] T. Jardin and L. David. Spanwise gradients in flow speed help stabilize leading-edge vortices on revolving wings. *Phys Rev E*, 90(1):013011, 2014. doi: 10.1103/PhysRevE.90.013011.

[7] D. Lentink, W. B. Dickson, J. L. van Leeuwen, and M. H. Dickinson. Leading-edge vortices elevate lift of autorotating plant seeds. *Science*, 324(5933):1438–1440, 2009. doi: 10.1126/science.1174196.

[8] F. T. Muijres, L. C. Johansson, R. Barfield, M. Wolf, G. R. Spedding, and A. Hedenström. Leading-Edge Vortex Improves Lift in Slow-Flying Bats. *Science*, 319(5867):1250–1253, 2008. doi: 10.1126/science.1153019.

[9] D. Lentink, U. K. Müller, E. J. Stamhuis, R. de Kat, W. van Gestel, L. L. M. Veldhuis, P. Henningsson, A. Hedenström, J. J. Videler, and J. L. van Leeuwen. How swifts control their glide performance with morphing wings. *Nature*, 446(7139):1082–1085, 2007. doi: 10.1038/nature05733.

[10] T. Y. Hubel and C. Tropea. The importance of leading edge vortices under simplified flapping flight conditions at the size scale of birds. *J Exp Biol*, 213(11):1930–1939, 2010. doi: 10.1242/jeb.047886.

[11] I. Borazjani and M. Daghooghi. The fish tail motion forms an attached leading edge vortex. *Proc R Soc B*, 280:20122071, 2013. doi: 10.1098/rspb.2012.2071.

[12] I. Gursul, R. Gordnier, and M. Visbal. Unsteady aerodynamics of nonslender delta wings. *Prog Aerosp Sci*, 41(7):515–557, 2005. doi: 10.1016/j.paerosci.2005.09.002.

[13] I. Gursul, Z. Wang, and E. Vardaki. Review of flow control mechanisms of leading-edge vortices. *Prog Aerosp Sci*, 43(7-8):246–270, 2007. doi: 10.1016/j.paerosci.2007.08.001.

[14] T. C. Corke and F. O. Thomas. Dynamic stall in pitching airfoils: Aerodynamic damping and compressibility effects. *Annu Rev Fluid Mech*, 47:479–505, 2015. doi: 10.1146/annurev-fluid-010814-013632.

[15] J. W. Larsen, S. R. K. Nielsen, and S. Krenk. Dynamic stall model for wind turbine airfoils. *J Fluid Struct*, 23 (7):959–982, 2007. doi: 10.1016/j.jfluidstructs.2007.02.005.

[16] I. M. Viola, S. Bartesaghi, T. Van-Renterghem, and R. Ponzini. Detached eddy simulation of a sailing yacht. *Ocean Eng*, 90:93–103, 2014. doi: 10.1016/j.oceaneng.2014.07.019.

[17] F. Bethwaite. *High Performance Sailing*. Waterline Books, UK, 1993.

[18] I. M. Viola and R. G. J. Flay. Force and pressure investigation of modern asymmetric spinnakers. *International Journal of Small Craft Technology Transaction RINA Part B2*, 151(2):31–40, 2009. doi: 10.3940/rina.ijsct.2009.b2.98.

[19] I. M. Viola and R. G J Flay. Pressure distributions on modern asymmetric spinnakers. *International Journal of Small Craft Technology Transaction RINA Part B1*, 152 (1):41–50, 2010. doi: 10.3940/rina.ijsct.2010.b1.103.

[20] P. Bot, I. M. Viola, R. G. J. Flay, and J.-S. Brett. Wind-tunnel pressure measurements on model-scale rigid downwind sails. *Ocean Eng*, 90:84–92, 2014. doi: 10.1016/j.oceaneng.2014.07.024.

[21] I. M. Viola and R. G. J. Flay. Sail pressures from full-scale, wind-tunnel and numerical investigations. *Ocean Eng*, 38(16):1733–1743, 2011. doi: 10.1016/j.oceaneng.2011.08.001.

[22] I. M. Viola and R. G. J. Flay. Sail aerodynamics: on-water pressure measurements on a downwind sail. *J Ship Res*, 56(4):197–206, 2012. doi: 10.5957/JOSR.56.4.110003.

[23] R. E. Gordnier, M. R. Visbal, I. Gursul, and Z. Wang. Computational and experimental investigation of a non-slender delta wing. *AIAA J*, 47(8):1811–1825, 2009. doi: 10.2514/1.37848.

[24] M. Honkanen and H. Nobach. Background extraction from double-frame PIV images. *Exp Fluids*, 38(3):348–362, 2005. doi: 10.1007/s00348-004-0916-x.

[25] L. Graftieaux, M. Michard, and N. Grosjean. Combining PIV, POD and vortex identification algorithms for the study of unsteady turbulent swirling flows. *Meas Sci Technol*, 12(1201):1422–1429, 2001. doi: 10.1088/0957-0233/12/9/307.

[26] C. E. Morgan, H.r Babinsky, and J. K. Harvey. Vortex detection methods for use with PIV and CFD data. In *47th AIAA Aerospace Sciences Meeting*, Orlando, Florida, 2009. doi: 10.2514/6.2009-74.

[27] J. Rabinovitch, V. Brion, and G. Blanquart. Effect of a splitter plate on the dynamics of a vortex pair. *Phys Fluids*, 24(7), 2012. doi: 10.1063/1.4737878.

[28] R. R. Harbig, J. Sheridan, and M. C. Thompson. Reynolds number and aspect ratio effects on the leading-edge vortex for rotating insect wing planforms. *J Fluid Mech*, 717:166–192, 2013. doi: 10.1017/jfm.2012.565.

[29] C. Pitt Ford and H. Babinsky. Lift and the leading-edge vortex. *J Fluid Mech*, 720:280–313, 2013. doi: 10.1017/jfm.2013.28.

[30] R. R. Harbig, J. Sheridan, and M. C. Thompson. Relationship between aerodynamic forces, flow structures and wing camber for rotating insect wing planforms. *J Fluid Mech*, 730:52–75, 2013. doi: 10.1017/jfm.2013.335.

6 AUTHORS BIOGRAPHY

Dr Ignazio Maria Viola is Senior Lecturer at the Institute for Energy Systems of the School of Engineering, University of Edinburgh and a Fellow of the Royal Institution of Naval Architects. He is Editor-in-Chief of the Journal of Sailing Technology (SNAME), and Member of the Editorial Board of Ocean Engineering (Elsevier) and the International Journal of Small Craft Technology (RINA). His background is in yacht sail aerodynamics, and his current research focuses on the control of vortical flow structures by means of flexible surfaces. He wrote more than 100 scientific publications and was awarded two RINA Medals of Distinctions and a RINA Medal of Exceptional Merit.

Abel Arredondo-Galeana is a PhD student at the University of Edinburgh, working under the supervision of Dr Viola. He has a background in Mechatronics Engineering and industrial experience as a wireline field engineer in the oil and gas industry. He was awarded a masters degree with honours in Sustainable Energy Systems at the University of Edinburgh in 2014. His thesis aimed at the developing a novel experimental rig for testing model-scale self-damping Flettner rotors for wind-assisted ship propulsion. Successively, he was funded a scholarship by the Consejo Nacional de Ciencia y Tecnología (CONACYT) to pursue his PhD project. His research aims to gain new insights on the vortex flow of yacht sails to enhance sail performances by design.